THE EUROPEAN
PHYSICAL JOURNAL C

Light yield of cold undoped CsI crystal down to 13 keV and the application of such crystals in neutrino detection

Keyu Ding[1], **Dmitry Chernyak**[1], **Jing Liu**[1,a]

[1] Department of Physics, University of South Dakota, 414 East Clark Street, Vermillion, SD 57069, USA

Abstract The light yield of an undoped CsI crystal at about 77 Kelvin was measured to be 33.5 ± 0.7 photo-electrons (PE) per keV electron-equivalent (keVee) in the energy range of [13, 60] keVee using X and γ-rays from an ^{241}Am radioactive source. Based on this experimental result, the performance of 10 kg cryogenic inorganic scintillating crystals coupled to SiPM arrays to probe non-standard neutrino interactions through the detection of coherent elastic neutrino-nucleus scatterings at the spallation neutron source, Oak Ridge National Laboratory, was examined in detail.

1 Introduction

43 years after Freedman predicted the existence of CEvNS [1], it was finally observed on experiments by the COHERENT collaboration at the SNS, ORNL, in 2017 [2]. The result has triggered significant interest, because it confirmed a long-predicted standard interaction important in the evolution of astronomical objects [3], and more importantly, it demonstrates the possibility to probe a broad range of standard and new physics through the detection of low energy neutrino interactions, including nuclear form factors [4,5], weak mixing angle [6] at low energies, neutrino electromagnetic interactions [7–10], sterile neutrinos [11], and NSIs [12–19], etc.

NSIs, first mentioned by Wolfenstein in his paper introducing the matter effect on neutrino oscillations in 1978 [20], can be categorized into two types: neutral-current (NC) and charge-current (CC) NSIs. The Lagrangian of the former can be expressed as [15]

$$\mathscr{L}_{\mathrm{NC}} = -2\sqrt{2}G_F \sum_{f,P,\alpha,\beta} \varepsilon_{\alpha\beta}^{f,P}(\bar{\nu}_\alpha\gamma^\mu P_L\nu_\beta)(\bar{f}\gamma_\mu Pf), \quad (1)$$

where G_F is the Fermi constant, f is one of the charged fermions in $\{e, u, d\}$, $\{\alpha, \beta\}$ are flavor indices, $P \in \{P_L, P_R\}$ are the chirality projection operators, which can be parameterized into vectors, V, and axial, A, components of the interaction. The ε terms quantify the strength of the new interaction, G_X, with respect to the Fermi constant, $\varepsilon_{\alpha\beta}^{f,P} \sim \mathcal{O}(G_X/G_F)$.

CC NSIs generally affect the production and detection of neutrinos; NC NSIs affect the neutrino propagation in matter [19], their introduction into the standard 3×3 neutrino mass and mixing scheme can hence change the whole picture of neutrino oscillation phenomenology, such as causing degeneracies in the measurement of the solar mixing angle [21], deriving the CP-violating phase δ_{CP} [22,23], mass hierarchy [24], etc. at current and future long-baseline neutrino experiments, such as DUNE [14,15,22].

Given such importance of NSIs, however, oscillation experiments are not sensitive to the terms that involve no flavor changing (or non-universal terms), $\varepsilon_{\alpha\alpha}^{f,P}$, which can be constrained better by neutrino scattering experiments, such as COHERENT. A sizable $\varepsilon_{\alpha\alpha}^{f,P}$ will cause a change of the number of CEvNS events. One can hence estimate its significance by comparing the observed number of CEvNS events to that predicted by the Standard Model (SM).

In addition to helping pin down NSI parameters not constrained by neutrino oscillation experiments, the stringent constraint on NSIs can also help with direct dark matter detection experiments [25]. As the sensitivities of those experiments improves, coherent scatterings of solar neutrinos in their targets become a serious background (the so-called *neutrino floor*) [26]. In determining the level of the floor, the introduction of NSIs results in an additional source of uncertainty [19]. The reduction of this uncertainty would consequently improve the sensitivity of direct dark matter search experiments deep underground.

The SNS at ORNL provides the world's most intense pulsed source of neutrinos [27] in an energy region of specific

Dmitry Chernyak: Now at the Department of Physics and Astronomy, University of Alabama, Tuscaloosa, AL, USA.

ᵃ e-mail: jing.liu@usd.edu (corresponding author)

interest for particle and nuclear astrophysics as a by-product of neutrons. Interactions of a proton beam in a mercury target produce π^+ and π^- in addition to neutrons. These pions quickly stop inside the dense mercury target. Most of π^- are absorbed. In contrast, the subsequent π^+ decay-at-rest (DAR) produces neutrinos of three flavors. The COHERENT experiment [27] is an ensemble of neutrino detectors located along the Neutrino Alley [2,27] about 20 m away from the source. Data taken with a 14 kg CsI(Na) detector [2] and a 24 kg (active) liquid argon detector [28] by the COHERENT Collaboration have already placed strong constrains on NSIs [2,28].

The sensitivity of an inorganic scintillator based detector can be improved by the increase of the target mass and the decrease of its energy threshold as more CEvNS events are expected at lower energies [1,2,13,28]. The two largest limiting factors in reducing the energy threshold of the CsI(Na) detector are [2], first, the Cherenkov radiation from charged particles passing through the quartz window of the photo-multiplier tube (PMT) directly coupled to the CsI(Na) crystal, and second, the afterglow of the crystal itself after some bright scintillation events.

The first limiting factor can be eliminated by replacing the PMT with silicon photomultiplier (SiPM) arrays, which do not have a quartz window. However, SiPMs operated at room temperature exhibit much higher dark count rates (DCR) than PMTs [29]. In order to reduce the DCR of SiPMs, they need to be cooled [30–35], for example by liquid nitrogen (LN2). The cryogenic operation calls for undoped CsI/NaI rather than doped ones, since the former at 77 K have about twice the light yields of the latter at 300 K [36–59]. The authors measured the light yield of undoped CsI at 77 K [58,60] and recently achieved a yield of ~26 PE/keVee using a cryogenic PMT with a peak quantum efficiency (QE) of ~27%. A light yield of 40~50 PE/keVee is achievable if PMTs are replaced by SiPMs with a peak photon detection efficiency (PDE) of 40~50%, which are already available in the market. Note that scintillation emitted from undoped NaI and CsI peak at 303 and 370 nm, respectively, while typical SiPMs are mostly sensitive to ~420 nm photons. Coating of wavelength-shifting materials, such as TPB, on SiPM surfaces is necessary for better light collection efficiency.

However, the high yields were measured at an energy range from 662 to 2614 keVee [58,60], far from the region that is relevant to the CEvNS detection (below 5 keVee). Evidence already exists of the non-linear scintillation responses of undoped NaI [54] and CsI [53] crystals. A measurement of the light yield at a lower energy region is needed to verify the feasibility of using undoped NaI and CsI at 77 K for CEvNS and NSI detection.

Reported in this paper is such a measurement using an undoped CsI crystal at 77 K with an ^{241}Am source down to 13 keVee. Based on the measured light yield, a design of a ~ 10 kg undoped CsI prototype detector located ~ 20 m away from the SNS for the detection of NSIs is presented. The sensitivity of such a prototype to low-mass dark matter particles possibly produced at the SNS has been presented in Ref. [60]. Its sensitivity to NSIs will be presented together with that of a future COHERENT liquid argon detector in another publication soon.

2 Light yield of undoped CsI down to 13 keVee

2.1 Experimental setup

Figure 1 shows the internal structure of the experimental setup for the measurement of the light yield of an undoped CsI crystal. The undoped cylindrical crystal was purchased from OKEN [61], and had a radius of 1 in. and a height of 1 cm. All surfaces were mirror polished. It was used in an earlier measurement, where a yield of 20.4 ± 0.8 PE/keVee was achieved above 662 keVee [58]. Compared to the early measurement, the following modifications were made:
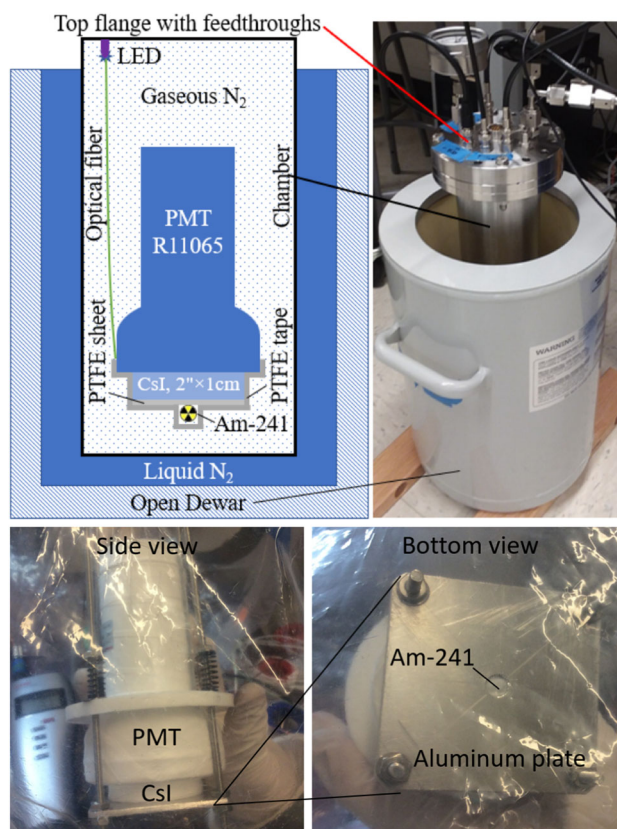
Fig. 1 A sketch and pictures of the experimental setup

- The side surface of the crystal was wrapped with multiple layers of Teflon tapes instead of a single layer to make sure that there was no light leak.
- The 2-in. Hamamatsu PMT R8778MODAY(AR) was replaced by a Hamamatsu 3-in. R11065-ASSY.
- In both setups, the PMTs were pushed against one of the crystal end surfaces by springs to ensure adequate optical contact without optical grease. However, in the previous setup, the crystal was pushed against the bottom flange of the chamber, while in this setup, the crystal was pushed against an aluminum plate with a hole in the middle, leaving space for the placement of an ^{241}Am source.
- The other end surface of the crystal was pushed against a PTFE sheet in between the crystal and the aluminum plate. The ^{241}Am source was placed on the other side of the PTFE sheet so that alpha radiation was blocked from reaching the crystal.

To minimize exposure of the crystal to atmospheric moisture, assembly was done in a glove bag flushed with dry nitrogen gas. The relative humidity was kept below 5% at 22 °C during the assemble process.

The PMT-crystal assemble was lowered into a 50 cm long stainless steel chamber from its top opening. The inner diameter of the chamber was ∼ 10 cm. The chamber was vacuum sealed on both ends by two 6-in. ConFlat (CF) flanges. The bottom flange was blank and attached to the chamber with a copper gasket in between. The top flange was attached to the chamber with a fluorocarbon CF gasket in between for multiple operations. Vacuum welded to the top flange were five BNC, two SHV, one 19-pin electronic feedthroughs and two 1/4-in. VCR connectors.

After all cables were fixed beneath it, the top flange was closed. The chamber was then pumped with a Pfeiffer Vacuum HiCube 80 Eco to ∼ 1 × 10^{-4} mbar. Afterward, it was refilled with dry nitrogen gas to 0.19 MPa above the atmospheric pressure and placed inside an open LN2 dewar. The dewar was then filled with LN2 to cool the chamber and everything inside. After cooling, the chamber pressure was reduced to slightly above the atmospheric pressure.

A few Heraeus C 220 platinum resistance temperature sensors were used to monitor the cooling process. They were attached to the side surface of the crystal, the PMT, and the top flange to obtain the temperature profile of the long chamber. A Raspberry Pi 2 computer with custom software [62] was used to read out the sensors. The cooling process took about 30 min. Most measurements, however, were taken after about an hour of waiting to let the system reach thermal equilibrium. The temperature of the crystal during measurements was about 3 K higher than the LN2 temperature.

The PMT was powered by a CAEN N1470A high voltage power supply in a NIM crate. The signals were fed into a CAEN DT5751 waveform digitizer, which had a 1 GHz sampling rate, a 1 V dynamic range and a 10 bit resolution. Custom-developed software was used for data recording [63]. The recorded binary data files were converted to CERN ROOT files for analysis [64].

2.2 Single PE response

The single-PE response of the PMT was measured using light pulses from an ultraviolet LED, LED370E from Thorlabs. Its output spectrum peaked at 375 nm with a width of 10 nm, which was within the 200–650 nm spectral response range of the PMT. Light pulses with a ∼50 ns duration and a rate of 10 kHz were generated using an RIGOL DG1022 arbitrary function generator. The intensity of light pulses was tuned by varying the output voltage of the function generator so that only one or zero photon hit the PMT during the LED lit window most of the time. A TTL trigger signal was emitted from the function generator simultaneously together with each output pulse. It was used to trigger the digitizer to record the PMT response. The trigger logic flow chart is shown in Fig. 2.

The PMT was biased at 1600 V, slightly above the recommended operation voltage, 1500 V, to increase the gain of the PMT. Single-PE pulses were further amplified by a factor of ten using a Phillips Scientific Quad Bipolar Amplifier Model 771 before being fed into the digitizer in order to separate them well from the pedestal noise.
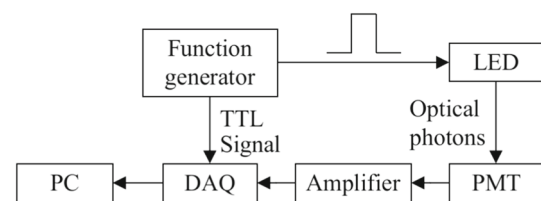
Fig. 2 Trigger logics for the PMT single-PE response measurements
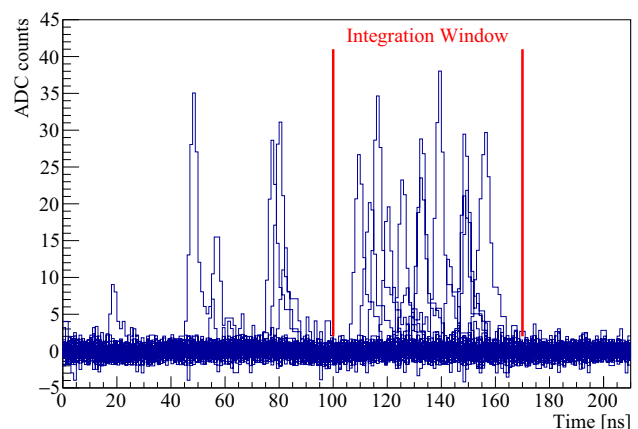
Fig. 3 Two hundred consecutive waveforms from the PMT overlapped with each other measured with the crystal in place
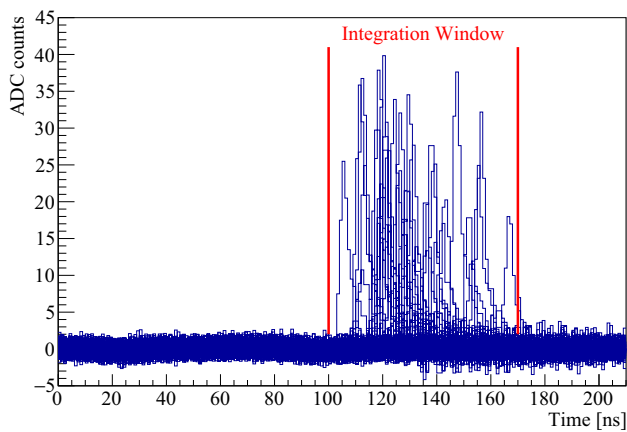
Fig. 4 Two hundred consecutive waveforms from the PMT overlapped with each other measured without the presence of the crystal

Fig. 5 Single PE response of the PMT in logarithm scale

Figure 3 shows two hundred consecutive waveforms from the PMT randomly selected from a single-PE response measurement. The integration window marked in the figure coincided with the LED lit window. Some single-PE pulses could be seen outside of the window. They were thought to be due to scintillation of random low energy radiation in the crystal.

To verify this assumption, the same measurement was repeated without the presence of the crystal. The resulting waveforms are shown in Fig. 4, where no pulse outside of the integration window can be seen.

An integration in this time window was performed for each waveform in the data file whether it contained a pulse or not. The resulting single-PE spectrum is shown in Fig. 5. The location of the single-PE peak varied within 5% in different measurements. In the energy calibration measurement to be mentioned in a later section, the single-PE spectrum with the crystal was used but with a 5% uncertainty attached to be conservative.
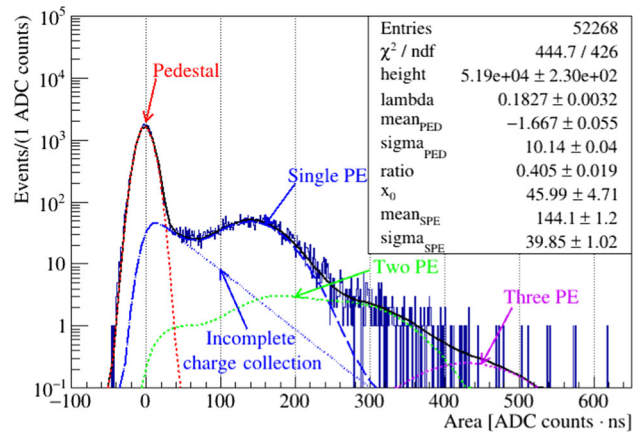
The spectrum was fitted in the same way as described in Ref. [65] with a function,

$$F(x) = H \sum_n P(n, \lambda) f_n(x), \qquad (2)$$

where H is a constant to match the fit function to the spectrum counting rate, $P(n, \lambda)$ is a Poisson distribution with a mean of λ, which represents the average number of PE in the time window, $f_n(x)$ represents the n-PE response, and can be expressed as

$$f_n(x) = f_0(x) * f_1^{n*}(x), \qquad (3)$$

where $f_0(x)$ is a Gaussian function representing the pedestal noise distribution, $*$ denotes a mathematical convolution of two functions, and $f_1^{n*}(x)$ is a n-fold convolution of the PMT single-PE response function, $f_1(x)$, with itself. The single-PE response function $f_1(x)$ was modeled as:

Table 1 Summary of single-PE response measurements before and after the energy calibration to be mentioned in the next section

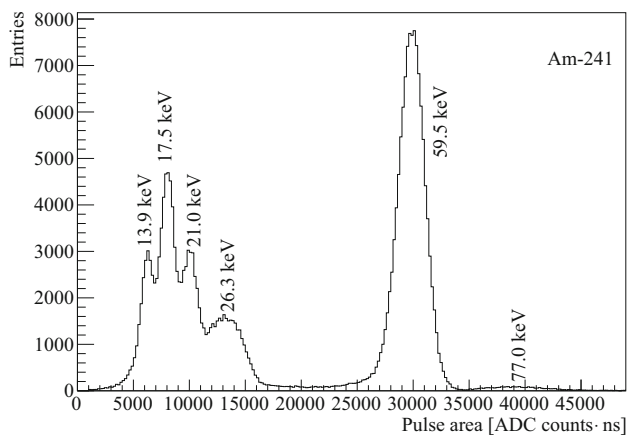|	Temperature of PMT (°C)	Temperature of crystal (°C)	Mean$_{SPE}$ (ADC counts×ns)
Before	-193.8 ± 1.1	-195.7 ± 1.1	14.58 ± 0.73
After	-192.8 ± 1.1	-193.7 ± 1.1	14.41 ± 0.72

$$f_1(x) = \begin{cases} R(\frac{1}{x_0}e^{-x/x_0}) + (1 - R)G(x; \bar{x}, \sigma) & x > 0; \\ 0 & x \leq 0, \end{cases} \qquad (4)$$

where R is the ratio between an exponential decay with a decay constant x_0, and a Gaussian distribution $G(x; \bar{x}, \sigma)$ with a mean of $\bar{x}$ and a width of σ. The former corresponds to the incomplete dynode multiplication of secondary electrons in the PMT. The latter corresponds to the full charge collection in the PMT.

The fitting function has eight free parameters as shown in the top-right statistic box in Fig. 5, where "height" corresponds to H in Eq. 2, "lambda" corresponds to λ in Eq. 2, "mean" and "sigma" with a subscript "PED" represents the mean and the sigma of the Gaussian pedestal noise distribution, those with a subscript "SPE" represents $\bar{x}$ and σ in Eq. 4, respectively, and "ratio" corresponds to R in Eq. 4. Due to technical difficulties in realizing multiple function convolutions in the fitting ROOT script, the three-PE distribution, $f_1^{3*}(x)$, was approximated by a Gaussian function with its mean and variance three times that of the single-PE response.

Table 1 lists the Gaussian means of single-PE distributions measured before and after the energy calibration to be mentioned in the next section to check the stability of the PMT gain. The average mean for the PMT at 1600 V is 14.5 ± 0.73 ADC counts·ns after being divided by the amplification factor, 10.

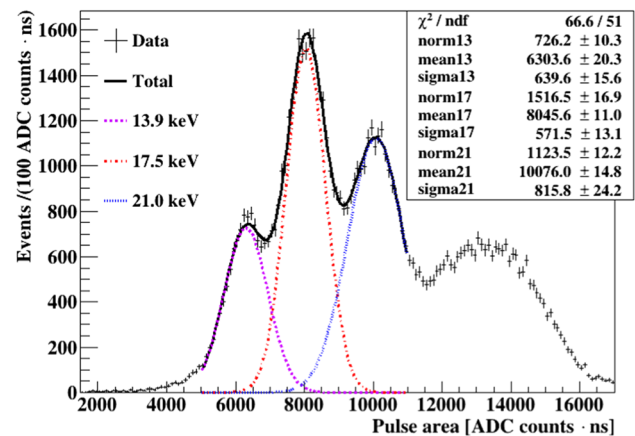**Fig. 6** Energy spectrum of ^{241}Am in the unit of ADC counts·ns

Fig. 7 Simultaneous fitting of the 13.9, 17.5 and 21.0 keV X-ray peaks with three Gaussian functions

Fig. 8 Simultaneous fitting of the 17.5, 21.0 keV X-ray and 26.3 keV γ-ray peaks with three Gaussian functions

2.3 Energy calibration

The energy calibration was performed using X and γ-rays from an ^{241}Am radioactive source [66,67]. The source was separated from the crystal by a PTFE sheet in between as shown in Fig. 1 so that α particles from the source could be blocked. The digitizer was triggered when the height of a pulse from the PMT was more than 5 ADC counts. As can be seen in Figs. 3 and 4, the typical height of a single PE pulse was around 20 ADC counts, and the baseline fluctuation was mostly within ± 3 ADC counts. The trigger threshold of 5 ADC counts could hence suppress most of the electronic noise spikes while let pass most of the single PE pulses. The trigger rate was ~ 6.3 kHz when the threshold was set to this value.

Each recorded waveform was 8008 ns long with a sampling rate of 1 GHz. About 1600 ns pre-traces were preserved before the rising edge of a pulse that triggered the digitizer so that there were enough samples before the pulse to calculate the averaged pedestal value of the waveform. After the pedestal was adjusted to zero the pulse was integrated until its tail fell back to zero. The integration had a unit of ADC counts·ns. The recorded energy spectrum in this unit is shown in Fig. 6.

The energy and origin of each peak were identified and summarized in Table 2, based on Ref. [66] and the *Table of Radioactive Isotopes* [67]. The energy resolution achieved here is very similar to that of a typical NaI(Tl) detector at room temperature [68].

Peaks in Fig. 6 were fitted with combinations of simple functions as shown in Figs. 7, 8, 9 and 10 to extract their mean values and widths. Uncertainties shown in the figures are only from the fitting processes. No systematical error is included. The X-ray peaks at 13.9, 17.5 and 21.0 keV were fitted with three Gaussian distributions simultaneously (Fig. 7), so were the 17.5, 21.0 and 26.3 keV peaks (Fig. 8). The 59.5 and
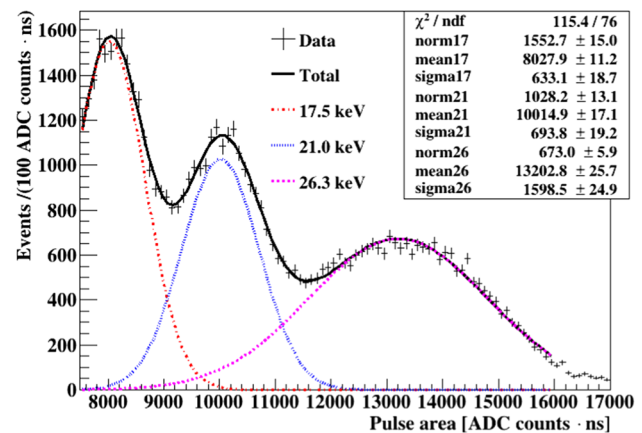
77.0 keV peaks were fitted with two Gaussian distributions on top of a horizontal line, the height of which was determined by the high energy side band of the 77.0 keV peak before the fitting (Figs. 9 and 10). Part of the low energy side of the 59.5 keV peak was excluded from the fitting since it cannot be described by a pure Gaussian distribution (Fig. 9). A Geant4-based Monte Carlo simulation [69] revealed the origin of the tail on the low energy side of the 59.5 keV peak to be γ-rays that lost part of their energies in the source encapsulation and the PTFE plate in between the source and the crystal.

As shown in Fig. 10, a different fitting method was tried for the 59.5 keV peak to verify the mean determined by the partial Gaussian fitting (Fig. 9). Parameters of the function are used to describe the 77.0 keV peak, and its side bands were obtained from the third fitting and fixed in this fitting. The left side of the 59.5 keV peak was partially described by a step function associated with the Gaussian function [70]
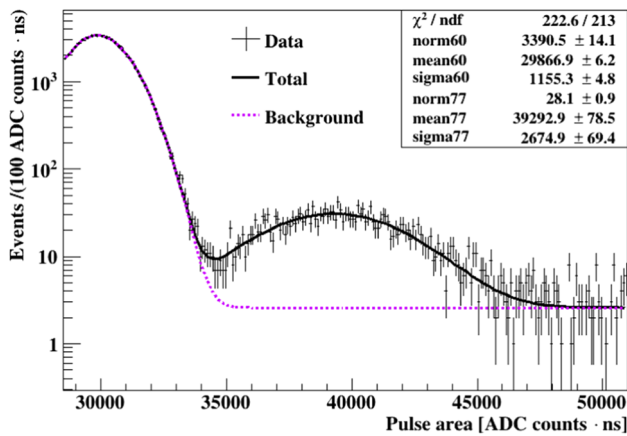
Fig. 9 Gaussian fitting of the 77 keV peak on top of a flat background and the tail of the 59.5 keV peak
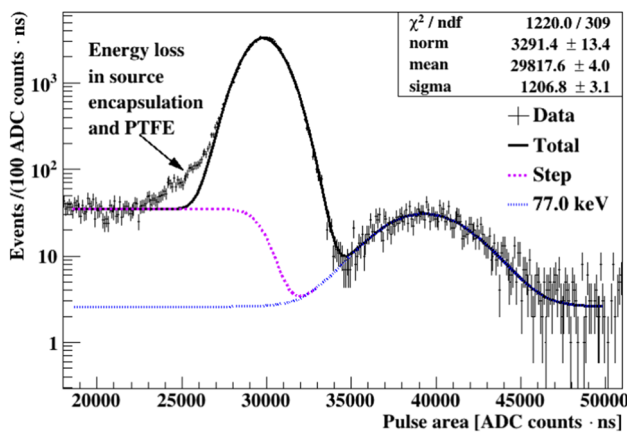

Fig. 10 Gaussian fitting of the 59.5 keV γ-ray peak on top of a flap background, the tail of the 77 keV peak and a smeared step function

used to fit the 59.5 keV peak:

$$N_0 \, \mathrm{erfc}\left(\frac{x - \bar{x}}{\sigma}\right) + N_1 \exp\left(\frac{(x - \bar{x})^2}{2\sigma^2}\right), \qquad (5)$$

where the height of the step, N_0, was determined by the left side band of the 59.5 keV peak and fixed in the fitting. The normalization factor, N_1, the mean, $\bar{x}$ and the width, σ, of the Gaussian function were determined by the fitting. The difference of the means determined in these two methods is less than 0.2%, the difference of the widths is less than 5%. The parameters obtained from the last fitting method were listed in Table 2 and used for the later analysis.

2.4 Light yield

The fitted means and widths of the X and γ-ray peaks in the ^{241}Am spectrum in the unit of ADC counts·ns were converted

to the number of PE using the formula:

$$(\text{number of PE}) = (\text{ADC counts} \cdot \text{ns})/\bar{x}, \qquad (6)$$

where $\bar{x}$ is the mean of the single-PE Gaussian distribution mentioned in Eq. 4, also in the unit of ADC counts·ns. An alternative choice would be to use the mean of $f_1(x)$ instead of $\bar{x}$ in Eq. 6. Since the mean of $f_1(x)$ is smaller than $\bar{x}$, such a choice would result in a larger light yield. The results shown here are hence conservative.

The light yield was calculated using the data in Table 2 and the following equation:

$$\text{light yield [PE/keVee]} = \frac{\text{Mean [number of PE]}}{\text{Energy [keVee]}}. \qquad (7)$$

The obtained light yield at each energy point is shown in Fig. 11. The error bars are mainly due to the uncertainty of the mean value of the single-PE response used to convert the x-axes of the energy spectra from ADC counts·ns to the number of PE. The data points were fitted with a straight line to get an average light yield, which is 33.5 ± 0.7 PE/keVee.

2.5 Non-linearity of light yield

The non-linearity of both undoped CsI [53] and NaI [54] at 77 K have been investigated from 5.9 keV to 1.3 MeV with rather small crystals (a few mm in all dimensions). The results vary with crystals used in those studies. Some had less, others had more light yields at lower energies than that at 1.3 MeV. The difference ranges from 0 to 30%. As mentioned in Sect. 2.1, in an earlier measurement with the same crystal used in this study, a yield of 20.4 ± 0.8 PE/keVee was obtained in the energy range of [662, 2614] keVee. One of the purposes of this study was to verify the light yield of this larger crystal at a lower energy range. Thanks to the multiple low energy X-rays from the ^{241}Am source, an even higher yield was achieved in the range of [13, 60] keVee. The non-linearity observed so far seems not a concern for the application of undoped CsI at 77 K in neutrino and dark matter detections.

3 Prototype detector at the SNS

Based on the measured light yield, the performance of a prototype detector made of ~ 10 kg undoped CsI or NaI crystals placed at the SNS, ORNL, was estimated. General considerations of such a prototype have been discussed in a previous publication [60]. They will be briefly summarized here together with a detailed reasoning of adopting SiPMs instead of cryogenic PMTs as light sensors for the proposed prototype.

Table 2 Fitting results of ^{241}Am peaks in the energy spectrum. The 13.9, 17.5 and 21.0 keV ones are obtained from the fitting shown in Fig. 7. The 26.3 keV ones are obtained from the fitting shown in Fig. 8. The 59.5 keV ones are obtained from the fitting shown in Fig. 10. The 77 keV ones are obtained from the fitting shown in Fig. 9

Type of radiation	Energy (keVee)	Mean (ADC·ns)	Sigma (ADC·ns)	FWHM (%)
X-ray	13.9†	6303.6	639.6	23.9
X-ray	17.5†	8045.6	571.5	16.7
X-ray	21.0†	10,076.0	815.8	19.1
γ-ray	26.3†	13,202.8	1598.5	28.5
γ-ray	59.5	29,817.6	1206.8	9.5
Sum‡	77.0	39,292.9	2674.9	15.9

†Intensity averaged mean of X or γ-rays near each other [66,67]
‡Sum of X-rays and 59.5 keV γ-ray
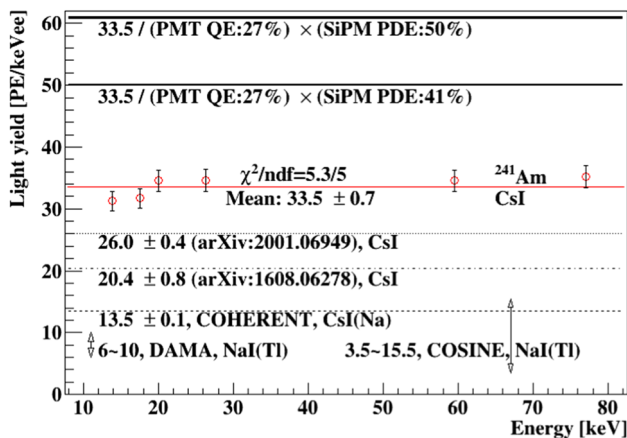
Fig. 11 Currently and previously achieved [58,60] light yields of undoped CsI at $\sim$ 77 K together with the predicted ones with SiPM as light sensors. Those of the COHERENT CsI(Na) [2], DAMA/LIBRA NaI(Tl) [71] and COSINE NaI(Tl) detectors [72] are plotted as well for comparison

3.1 Neutrino source

The SNS is the world's premier neutron-scattering research facility. At its full beam power, about 1.5×10^{14} 1 GeV protons bombard a liquid mercury target in 600 ns bursts at a rate of 60 Hz [27]. Neutrons produced in spallation reactions in the mercury target are thermalized in cryogenic moderators surrounding the target and are delivered to neutron-scattering instruments in the SNS experiment hall.

As a byproduct, the SNS provides the world's most intense pulsed source of neutrinos peaked around a few of tens MeV [27]. Interactions of the proton beam in the mercury target produce π^+ and π^- in addition to neutrons. These pions quickly stop inside the dense mercury target. Most of π^- are absorbed. In contrast, the subsequent π^+ decay-at-rest (DAR) produces neutrinos of three flavors.

The sharp SNS beam timing structure ($\sim$ 1 μs for prompt ν_μ, $\sim$ 10 μs for delayed ν_e and $\bar{\nu}_\mu$ [27]) is highly beneficial for background rejection and precise characterization of

those backgrounds not associated with the beam [73], such as those from radioactive impurities in a crystal. Looking for beam-related signals only in the 10 μs window after a beam spill imposes a factor-of-2000 reduction in the steady-state background.

The COHERENT Collaboration occupies the "Neutrino Alley" located $\sim$20 m from the mercury target with contiguous intervening shielding materials and overburden eliminating almost all free-streaming pathways for fast neutrons which dominate beam-related backgrounds. The prototype is assumed to be at the same location as the previous CsI (Na) detector.

3.2 Crystal target

About 10 kg undoped CsI operated at 77 K is assumed in this sensitivity analysis. Due to nearly identical scintillation mechanism and behavior ([60] and references therein), undoped NaI can be another candidate. Multiple targets would be an even better choice as different isotopes in the targets help verify the neutron number dependence of the CEvNS cross section [27]. The operation temperature is chosen for three reasons. The first is its convenience – LN2 cooling is conventional and economic. The second is to lower the DCR of SiPM arrays as a replacement of PMTs. This will be discussed in more detail in the following sections. The last is to utilize the high intrinsic light yields of undoped crystals at that temperature [36–59]. The target mass is chosen to be similar to that of the COHERENT CsI(Na) detector [2] for easy comparison. Crystals in such a mass range can also be used as an optical module in a larger detector. Figure 12 shows a simplified 3D drawing of such a module, where two opposite surfaces of a $10 \times 10 \times 10$ cm^3 crystal are covered by SiPM arrays, others are covered by PTFE light reflectors. The module with three cubic crystals can be directly submerged in LN2 or placed in a sealed chamber bathed in LN2.
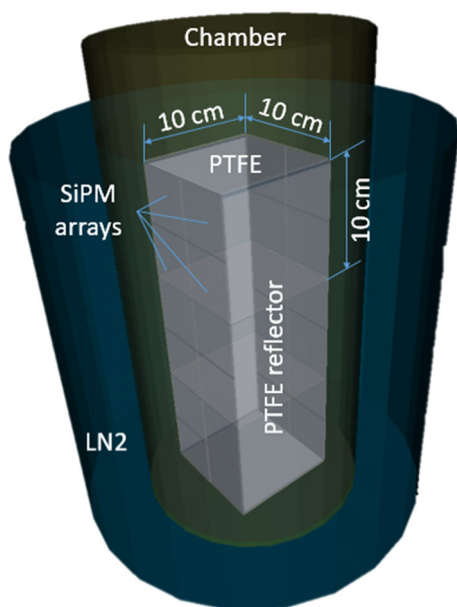
Fig. 12 A simplified 3D drawing of a ∼10 kg detector module

3.3 PMTs

As liquid noble gas based dark matter detectors advance, quite a few PMTs became available in the market, which can work at 77 K with a reasonable QE in the ultra-violet (UV) region, such as Hamamatsu R8778MODAY(AR) [74] and R11065, etc. [75]. Their performance in terms of light detection has been proven to be good enough in this and previous measurements [58,60]. For example, a 1-PE trigger threshold of a detector can be translated to ∼ 30 eVee in energy, given a light yield of 33.5 ± 0.7 PE/keVee. This is much lower than the threshold of any existing inorganic scintillating crystal based dark matter or neutrino experiment.

However, energetic charged particles from natural radiation and cosmic rays can generate Cherenkov radiation when they pass through a PMT quartz (or fused silica) window. Given enough energy, a Cherenkov event can be easily distinguished from a scintillation event, since the former happens in a much shorter time window (typically, a few nanoseconds) than the latter (typically, hundreds of nanoseconds [60]). The current pulse of the former is hence much sharper than that of the latter. However, close to the energy threshold, there are only a few detectable photons, which create a few single-PE pulses virtually identical in shape. The efficiency of pulse shape discrimination becomes lower and lower as the energy diminishes. This is demonstrated clearly in Fig. 13, the detection efficiency of CEvNS events near the energy threshold of the COHERENT CsI(Na) detector, adopted from Ref. [2]. The energy threshold of the detector was mainly limited by the Cherenkov event selection criterion instead of the light yield of the system.
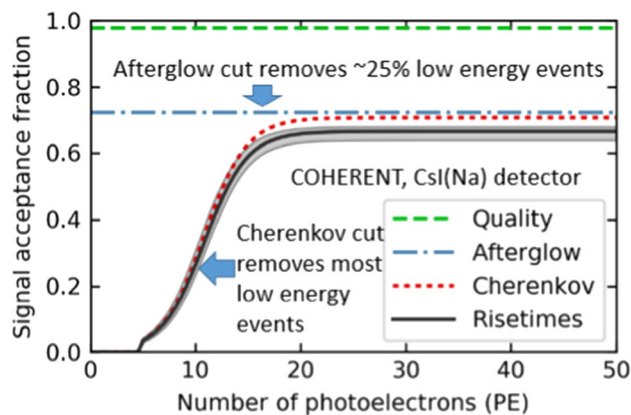
Fig. 13 Detection efficiency of low energy events after each event selection criterion of the COHERENT CsI(Na) detector, adopted from Ref. [2]. Cherenkov cut removes most of the events near threshold

In the COHERENT CsI(Na) detector, only one PMT was used. However, even if two PMTs are coupled to the two end surfaces of a cylindrical crystal, a request of coincident light detection in both of them cannot help remove Cherenkov events since the Cherenkov light created in one PMT can easily propagate to the other.

3.4 SiPM arrays

Two alternative sensors that do not generate Cherenkov radiation are avalanche photodiodes (APDs) and SiPMs. Made of silicon wafers, they can be much more radio-pure than PMTs, and do not need a thick SiO_2 window. APDs are a very attractive option [76] given their high PDE (∼80%). However, since they need to be operated in the linear mode, the gain is much less than those of PMTs and SiPMs, and cannot be triggered at single-PE level. On the other hand, a SiPM, which is basically an array of small APDs (micro cells) working in Geiger mode, is sensitive down to a single PE in each of its micro cell. The size of its micro cells has to be sufficiently small to avoid the situation when more than one photon hits the same micro cell. The space in between micro cells are not sensitive to photons. The peak PDE of a SiPM (up to 56% at this moment [35]) is hence smaller than that of an APD, but is typically higher than the peak QE of a PMT [77].

Since covering a large area with a monolithic SiPM die is not possible mainly due to the production yield, a compromised solution is to tile several dies tightly together to form an array. Given the same active area, a SiPM array uses less material, occupies less space, and can be made more radio-pure than a PMT. All of these properties make SiPMs very attractive light sensors. Table 3 lists a few SiPM arrays that are already available in the market. All have an PDE that is higher than that of a PMT. Their gains are also very close to that of a typical PMT, which makes the signal readout much

easier than that for an APD. More importantly, most of them have been tested in liquid argon or LN2 temperature (for example, Refs. [31,78–81] for SensL, Refs. [30,33,82] for Hamamatsu, and Ref. [83] for KETEK SiPMs). FBK SiPMs were proven working even down to 40 K with a good performance [34,35,84]. The light yield of the current system can be further improved by replacing PMTs (QE $\sim$ 27%) with SiPM arrays (PDE: 40–50%) to 50 or even 60 PE/keVee, shown as the top two lines in Fig. 11.

One major drawback of a SiPM array compared to a PMT is its high DCR at room temperature ($\sim$ hundred kHz). Fortunately, it drops quickly with temperature, and can be as low as 0.2 Hz/mm^2 below 77 K [34], while the PDE does not change much over temperature [30,78,82,85]. However, a SiPM array that has an active area similar to a 3-in PMT would still have an about 100 Hz DCR at 77 K. A simple toy MC reveals that a 10-ns coincident window between two such arrays coupled to the same crystal results in a trigger rate of about 10^{-5} Hz. A further time coincidence with the SNS beam pulses would make the rate negligible.

Afterpulses [29] resulted from delayed releases of trapped electrons in metastable traps in a SiPM can mimic low energy events. But, just as DCR, they can be suppressed efficiently once coincident triggers are required.

Secondary photons with a wavelength range from 450 to 1600 nm can be emitted isotropically from a fired cell in a SiPM. Some of them can travel to a neighboring cell and cause optical crosstalk [30,78,82,85]. All major manufacturers are actively improving their technologies to reduce the crosstalk rate, which ranges from 2 to 27% at this moment depending on the manufacturer, the size of micro cells, and the over-voltage applied. In general, smaller cell sizes and over-voltages cause less crosstalks but also smaller PDE.

However, the effect of optical crosstalk may be partially corrected for neutrino and dark matter induced low energy events close to the threshold, where the chance of one SiPM in an array to receive two photons at the same time is very low. By reading out individual SiPMs in an array, the pulse in a SiPM that is much larger than the pulse in any other SiPM has a high chance to be contaminated by crosstalk and can be regarded as a single PE.

The effectiveness of this correction was verified by a simple Geant4-based optical simulation [69], where 100,000 optical photons were emitted isotropically from a point inside a $10 \times 10 \times 10$ cm^3 cubic crystal, as shown in Fig. 14. The point was less than 1 mm away from the left surface fully covered by 16×16 SiPMs, each covered an area of 6.25×6.25 mm^2. The right surface was covered by the same amount of SiPMs. Other surfaces were covered by PTFE reflectors. The refraction and reflection rates on the interface between the crystal and SiPMs are determined by their refraction indices, 1.9 (CsI) and 1.52 (typical optical resin), respectively. A diffuse reflectivity of 99% was assumed for
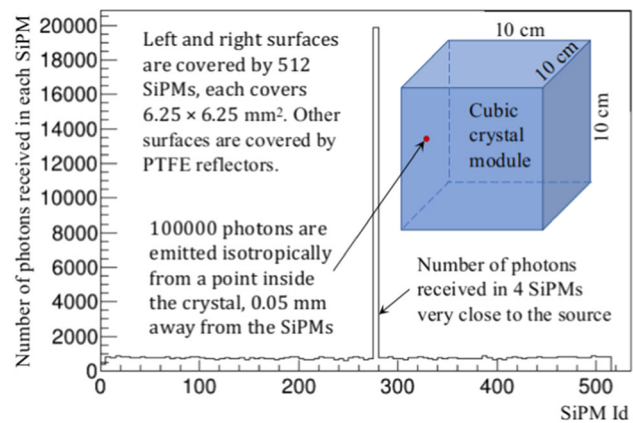
Fig. 14 Number of received photons by individual SiPMs attached to the left and right surfaces of a $10 \times 10 \times 10$ cm^3 crystal in a Geant4-based optical simulation, where 100,000 photons were emitted isotropically from the point shown in the figure

PTFE. Four SiPMs very close to the emission point were about 20 times more possible to receive a photon. However, the possibility for each of them receiving two photons at the same time is only $\sim (20,000/100,000)^2 = 4\%$. The possibility quickly dropped to nearly zero when the emission point was moved more than 1 mm away from the SiPM covered surface. Therefore, an analysis treatment that regards each triggered SiPM as having only a single PE effectively reduces the influence of optical crosstalk while sacrificing minimal signal.

To summarize, there are three major technical advantages in the combination of cryogenic undoped crystals with SiPM arrays:

– Cherenkov radiation from a PMT window is eliminated.
– Larger intrinsic light yields of cryogenic undoped crystals compared to those of doped ones at room temperature are utilized [60].
– Larger PDE of SiPM arrays compared to QE of PMTs is utilized.

Meanwhile, the major drawbacks of SiPM arrays, such as DCR, afterpulses and optical crosstalk, can be kept under control with a reasonable amount of effort.

3.5 Energy threshold

Without Cherenkov radiation from PMTs, the energy threshold of the prototype detector in terms of keVee is basically determined by its light yield. Assuming a conservative yield of 50 PE/keVee as shown in Fig. 11, and triggering on at least two photoelectrons in two different light sensors, the threshold can be roughly estimated as 2/50 = 40 eVee. To be more precise, a curve of trigger efficiency versus number of optical photons near the threshold was obtained with a

SiPM array	Microcell size (μm^2)	PDE[†] (%)	Largest array size (mm^2)	Gain[◇] ($\times 10^6$)
S[1] J-series	35×35	50	50.4×50.4	6.3
S[1] C-series	35×35	40	57.4×57.4	5.6
H[2] S141xx	50×50	50	25.8×25.8	4.7
H[2] S133xx	50×50	40	25.0×25.0	2.8
K[3] PM3325	25×25	43	26.8×26.8	1.7

[†] @ 420 ∼ 450 nm   [◇] @ 5 volt over-voltage
[1]SensL   [2]Hamamatsu   [3]KETEK
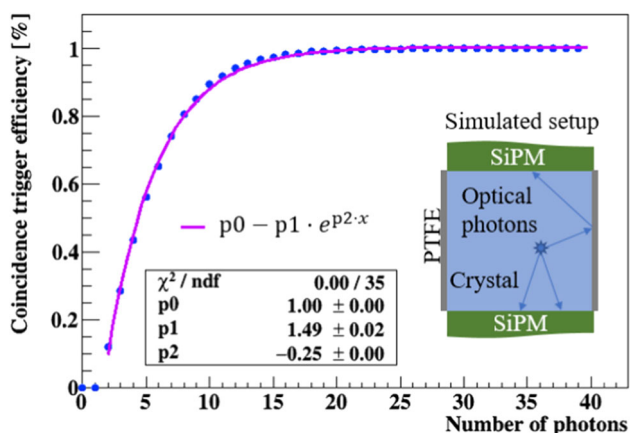
Fig. 15 Two-PE coincidence trigger efficiency as a function of the number of emitted photons in the proposed detector. Taken from Ref. [60]

toy Monte Carlo simulation detailed in Ref. [60], shown in Fig. 15. Based on the curve, the trigger efficiency is about 50% at 40 eVee.

3.6 Quenching factor

The energy threshold for neutrino or dark matter scattering events is not only determined by the light yield but also the scintillation quenching factor for nuclear recoils. There is no systematic measurement of quenching factors for undoped crystals in such a low energy region. Assuming a constant quenching factor of 0.08 for NaI and 0.05 for CsI, borrowed from measurements with doped crystals [2,86], the threshold of 40 eVee can be translated to 0.5 keV for Na recoils, and 0.8 keV for Cs recoils. Given completely different scintillation mechanisms [60] however, there is a possibility that scintillation quenching in undoped crystals is less serious than that in doped ones. For example, a very preliminary investigation [59] suggests a quenching factor of 0.1 for undoped CsI. More interestingly, a study of the quenching of alpha particles in an undoped CsI at a wide temperature range [87] revealed a 20% larger scintillation yield of alpha particles than electronic recoils at 77 K. A slight modification of the current experimental setup was tried to allow alpha particles

from the ^{241}Am source to reach the crystal. A similar increase in yield as that in Ref. [87] was observed. The result will be presented in another publication. All these initial investigations call for a more systematic study of the scintillation response of undoped crystals to various incident particles.

4 Conclusion

The light yield of an undoped CsI crystals at about 77 K was measured to be 33.5 ± 0.7 PE/keVee in the energy range of [13, 60] keVee using X and γ-rays from an ^{241}Am radioactive source. Compared to a previous measurement of 26 ± 0.4 PE/keVee in the range of [662, 2615] keVee [60], the energy range of this measurement was much closer to the range that is of great interest for the detection of NSIs and dark matter particles at the SNS, ORNL.

The performance of a 10 kg prototype detector based on cryogenic inorganic scintillating crystals coupled to SiPM arrays [60] to probe NSIs through CEvNS detection at the SNS, ORNL, was discussed after the description of the experimental result. The key technical advantages of the prototype include much higher light yields of undoped crystals at 77 K compared to those of doped ones at room temperature, and a complete elimination of Cherenkov radiation originated from PMTs that seriously limits the energy threshold of current inorganic scintillator detectors. Its sensitivity to NSI parameters will be published together with those from other COHERENT detector systems in a separate publication.

References

1. D.Z. Freedman, Phys. Rev. D **9**, 1389 (1974)
2. COHERENT Collaboration, D. Akimov, et al., Science, eaao0990 (2017)
3. H.T. Janka, K. Langanke, A. Marek, G. Martínez-Pinedo, B. Müller, Phys. Rep. **442**(1), 38 (2007)
4. K. Patton, J. Engel, G.C. McLaughlin, N. Schunck, Phys. Rev. C **86**(2), 024612 (2012)
5. K.M. Patton, G.C. McLaughlin, K. Scholberg, Int. J. Mod. Phys. E **22**(06), 1330013 (2013)
6. B.C. Cañas, E.A. Garcés, O.G. Miranda, A. Parada, Phys. Lett. B **784**, 159 (2018)
7. T.S. Kosmas, O.G. Miranda, D.K. Papoulias, M. Tórtola, J.W.F. Valle, Phys. Rev. D **92**(1), 013011 (2015)
8. A.G. Beda, V.B. Brudanin, E.V. Demidova, V.G. Egorov, D.V. Medvedev, M.V. Shirchenko, A.S. Starostin, T. Vylov, Phys. Part. Nucl. Lett. **7**(6), 406 (2010). arXiv:0906.1926
9. TEXONO Collaboration, Phys. Rev. D **75**(1), 012001 (2007)
10. Z. Daraktchieva, C. Amsler, M. Avenier, C. Broggini, J. Busto, C. Cerna, F. Juget, D.H. Koang, J. Lamblin, D. Lebrun, O. Link, G. Puglierin, A. Stutz, A. Tadsen, J.L. Vuilleumier, V. Zacek, Phys. Lett. B **615**(3), 153 (2005)
11. J.A. Formaggio, E. Figueroa-Feliciano, A.J. Anderson, Phys. Rev. D **85**(1), 013009 (2012)
12. S. Davidson, C.P. na Garay, N. Rius, A. Santamaria, J. High Energy Phys. **2003**(03), 011 (2003)
13. J. Barranco, O.G. Miranda, T.I. Rashba, J. High Energy Phys. **2005**(12), 21 (2005)
14. P. Coloma, T. Schwetz, Phys. Rev. D **94**(5), 055005 (2016)
15. P. Coloma et al., JHEP **2017**(4), 116 (2017)
16. J. Liao, D. Marfatia, Phys. Lett. B **775**, 54 (2017)
17. D.K. Papoulias, T.S. Kosmas, Phys. Rev. D **97**(3), 033003 (2018)
18. P.B. Denton, Y. Farzan, I.M. Shoemaker, *A Plan to Rule out Large Non-Standard Neutrino Interactions After COHERENT Data* (2018). arXiv:1804.03660
19. P.S.B. Dev, et al., *Neutrino Non-Standard Interactions: A Status Report* (2019). arXiv:1907.00991
20. L. Wolfenstein, Phys. Rev. D **17**(9), 2369 (1978)
21. O.G. Miranda, M.A. Tórtola, J.W.F. Valle, JHEP **2006**(10), 008 (2006)
22. J. Liao, D. Marfatia, K. Whisnant, Phys. Rev. D **93**(9), 093016 (2016)
23. L.J. Flores et al., Phys. Rev. D **98**(3), 035030 (2018)
24. K.N. Deepthi, S. Goswami, N. Nath, Phys. Rev. D **96**(7), 075023 (2017)
25. M. Schumann, J. Phys. G **46**(10), 103003 (2019)
26. J. Billard, L. Strigari, E. Figueroa-Feliciano, Phys. Rev. D **89**(2), 023524 (2014)
27. COHERENT Collaboration, D. Akimov, et al., *COHERENT 2018 at the Spallation Neutron Source* (2018). arXiv:1803.09183
28. COHERENT Collaboration, D. Akimov, et al., *First Detection of Coherent Elastic Neutrino-Nucleus Scattering on Argon* (2020). arXiv:2003.10630
29. G. Collazuol. *The SiPM Physics and Technology – a Review*. International Workshop on New Photon-detectors, PhotoDet 2012, June 13-15, 2012, LAL Orsay, France (2016). https://indico.cern.ch/event/164917/contributions/1417121/attachments/198512/278663/PhotoDet12_-_collazuol_-_v3.pdf. Accessed 5 Aug 2016
30. M. Akiba, K. Tsujino, K. Sato, M. Sasaki, Opt. Express **17**(19), 16885 (2009)
31. S. Catalanotti, A.G. Cocco, G. Covone, M. D'Incecco, G. Fiorillo, G. Korga, B. Rossi, S. Walker, J. Instrum. **10**(08), P08013 (2015)
32. I. Ostrovskiy et al., IEEE Trans. Nucl. Sci. **62**(4), 1825 (2015)
33. T. Igarashi, M. Tanaka, T. Washimi, K. Yorita, Nucl. Instrum. Methods A **833**, 239 (2016)
34. C.E. Aalseth et al., J. Instrum. **12**(09), P09030 (2017)
35. G. Giovanetti, *SiPM at Cryogenic Temperatures for Dark Matter Searches* (2017). https://indico.cern.ch/event/606690/contributions/2623443/ **15-th Int'l. Conf. Topics Astropart. Underground Phys**
36. J. Bonanomi, J. Rossel, Helv. Phys. Acta **25**(VII), 725 (1952)
37. E. Hahn, J. Rossel, Helv. Phys. Acta **26**, 271 (1953)
38. B. Hahn, J. Rossel, Helv. Phys. Acta **26**, 803 (1953)
39. W. Van Sciver, I.R.E. Trans, Nucl. Sci. **3**(4), 39 (1956)
40. L.E. Beghian, G.H.R. Kegel, R.P. Scharenberg, Rev. Sci. Instrum. **29**(9), 753 (1958)
41. W. Van Sciver, Phys. Rev. **120**(4), 1193 (1960)
42. M.P. Fontana, H. Blume, W.J. van Sciver, Phys. Status Solidi (b) **29**(1), 159 (1968)
43. J.B. West, A.J.L. Collinson, J. Phys. B **3**(10), 1363 (1970)
44. M.P. Fontana, W.J. van Sciver, Phys. Status Solidi (b) **37**(1), 375 (1970)
45. W.L. Emkey, P.V. Meyers, W.J. Van Sciver, J. Opt. Soc. Am. **66**(3), 264 (1976)
46. D.E. Persyk, M.A. Schardt, T.E. Moi, K.A. Ritter, G. Muehllehner, IEEE Trans. Nucl. Sci. **27**(1), 167 (1980)
47. C. Woody, P. Levy, J. Kierstead, T. Skwarnicki, Z. Sobolewski, M. Goldberg, N. Horwitz, P. Souder, D. Anderson, IEEE Trans. Nucl. Sci. **37**(2), 492 (1990)
48. R. Williams, K. Song, J. Phys. Chem. Solids **51**(7), 679 (1990)
49. J. Wear, J. Karp, A. Haigh, R. Freifelder, IEEE Trans. Nucl. Sci. **43**(3), 1945 (1996)
50. C. Amsler, D. Grögler, W. Joffrain, D. Lindelöf, M. Marchesotti, P. Niederberger, H. Pruys, C. Regenfus, P. Riedler, A. Rotondi, Nucl. Instrum. Methods A **480**(2), 494 (2002)
51. M. Moszyński, M. Balcerzyk, W. Czarnacki, M. Kapusta, W. Klamra, P. Schotanus, A. Syntfeld, M. Szawlowski, IEEE Trans. Nucl. Sci. **50**(4), 767 (2003)
52. M. Moszyński, W. Czarnacki, W. Klamra, M. Szawlowski, P. Schotanus, M. Kapusta, Nucl. Instrum. Methods A **504**(1–3), 307 (2003)
53. M. Moszyński, M. Balcerzyk, W. Czarnacki, M. Kapusta, W. Klamra, P. Schotanus, A. Syntfeld, M. Szawlowski, V. Kozlov, Nucl. Instrum. Methods A **537**(1), 357 (2005)
54. M. Moszyński, W. Czarnacki, A. Syntfeld-Kazuch, A. Nassalski, T. Szczęśniak, L. Swiderski, F. Kniest, A. Iltis, IEEE Trans. Nucl. Sci. **56**(3), 1655 (2009)
55. P. Sibczyński, M. Moszyński, T. Szczęśniak, W. Czarnacki, A. Syntfeld-Kazuch, P. Schotanus, in *IEEE Nucl. Sci. Sym. Med. Imag. Conf.* (IEEE, 2010), pp. 574–579
56. P. Sibczyński, M. Moszyński, T. Szczęśniak, W. Czarnacki, JINST **7**(11), P11006 (2012)
57. V.B. Mikhailik, V. Kapustyanyk, V. Tsybulskyi, V. Rudyk, H. Kraus, Phys. Status Solidi (b) **252**(4), 804 (2015)
58. J. Liu, M. Yamashita, A.K. Soma, J. Inst. **11**(10), P10003 (2016)

59. D. Baxter, et al., *Coherent Elastic Neutrino-Nucleus Scattering at the European Spallation Source* (2019). arXiv:1911.00762
60. D. Chernyak, D. Pershey, J. Liu, K. Ding, N. Saunders, T. Oli, Eur. Phys. J. C **80**(6), 547 (2020). https://doi.org/10.1140/epjc/s10052-020-8111-7
61. OKEN-OHYO Koken Kogyo Co., Ltd (2020). http://www.oken.jp/
62. J. Mammo, Josephss/CraViS (2018). https://github.com/Josephss/CraViS
63. J. Liu, jintonic/daq (2019). https://github.com/jintonic/daq
64. J. Liu, jintonic/nice (2020). https://github.com/jintonic/nice
65. T. Alexander et al., Astropart. Phys. **49**, 44 (2013)
66. J.L. Campbell, P.L. McGhee, Nucl. Instrum. Methdos A **248**(2), 393 (1986). https://doi.org/10.1016/0168-9002(86)91024-7
67. S. Chu, L. Ekström, R. Firestone, *WWW Table of Radioactive Isotopes* (2020). http://nucleardata.nuclear.lu.se/nucleardata/toi/. Database version 28 Feb 1999
68. G.F. Knoll, *Radiation Detection and Measurement* (Wiley, New York, 2010)
69. J. Liu, jintonic/gears (2020). http://physino.xyz/gears
70. Step background function (2020). http://www.hlabsoft.com/web/hl2005/referenceguide/20052b-html/step_background_function.htm
71. R. Bernabei et al., Nucl. Phys. At. Energy **19**(4), 307 (2018). https://doi.org/10.15407/jnpae2018.04.307
72. G. Adhikari et al., Phys. Rev. Lett. **123**, 031302 (2019)
73. A. Bolozdynya, et al. *Opportunities for Neutrino Physics at the Spallation Neutron Source: A White Paper* (2012). arXiv:1211.5199
74. M. Yamashita, (2010). http://w4.gakkai-web.net/jps_search/2010au/u.html#13aSG-1-1. Accessed on 5 Aug 2016 (**Talk in Annual Fall Meeting of Physical Society of Japan, 2010**)
75. Y. Hotta. Latest developments in PMTs for low temperature operation (2014). http://www.pa.ucla.edu/sites/default/files/webform/Hamamatsu%20Presentation%20for%20DM2014.pdf. Accessed 5 Aug 2016 **Talk in 11th Symposium on Sources and Detection of Dark Matter and Dark Energy in the Universe, February 26 – 28, 2014, Northwest Campus Auditorium at Covel Commons, UCLA**
76. D. Baxter et al., JHEP **2020**(2), 123 (2020)
77. C. Jackson, K. O'Neill, L. Wall, B. McGarvey, Opt. Eng. **53**(8), 081909 (2014)
78. P.K. Lightfoot, G.J. Barker, K. Mavrokoridis, Y.A. Ramachers, N.J.C. Spooner, J. Instrum. **3**(10), P10001 (2008)
79. P.K. Lightfoot, G.J. Barker, K. Mavrokoridis, Y.A. Ramachers, N.J.C. Spooner, JINST **4**(04), P04002 (2009)
80. B. Rossi et al., J. Inst. **11**(02), C02041 (2016)
81. C. Johnson, Qualification of silicon photomultipliers and readout boards for use in protodune photon detectors. Ph.D. thesis, Colorado State University (2018). https://mountainscholar.org/bitstream/handle/10217/189282/Johnson_colostate_0053N_14655.pdf
82. H. Otono, *Proceedings of International Workshop on New Photon-Detectors PD07* (2007)
83. J.J. Csáthy, T. Bode, J. Kratz, S. Schönert, C. Wiesinger, Optical fiber read-out for liquid argon scintillation light (2016). arXiv:1606.04254
84. F. Acerbi et al., IEEE Trans. Electron Dev. **64**(2), 521 (2017)
85. J. Janicskó Csáthy, H. Aghaei Khozani, A. Caldwell, X. Liu, B. Majorovits, Nucl. Instrum. Methods A **654**(1), 225 (2011)
86. J. Xu et al., Phys. Rev. C **92**(1), 015807 (2015)
87. M. Clark, P. Nadeau, S. Hills, C. Dujardin, P.C.F. Di Stefano, Nucl. Instrum. Methods A **901**, 6 (2018)